NANO LETTERS
Cite This: Nano Lett. 2020, 20, 166−175
Letter
pubs.acs.org/NanoLett

Fully Solid-State Graphene Transistors with Striking Homogeneity and Sensitivity for the Practicalization of Single-Device Electronic Bioassays

Cheng Wang,*[,†,‡] Jingjing Wu,[†,§] Yashuo He,[†,§] Ze Song,[†,∥] Sumeng Shi,[†,§] Yibo Zhu,[⊥] Yuan Jia,*[,#] and Weixiang Ye*[,▽]

[†]Tianjin Key Laboratory of Wireless Mobile Communications and Power Transmission, [‡]Department of Intelligence Science and Technology, [§]Department of Communication Engineering, and [∥]Department of Electronic Science and Technology, College of Electronic and Communication Engineering, Tianjin Normal University, Tianjin 300387, China

[⊥]Department of Mechanical Engineering, Columbia University, New York 10027, United States

[#]Jiangsu Key Laboratory of Micro-Nano Biomedical Instrument Design and Manufacture, School of Mechanical Engineering, Southeast University, Nanjing 211189, China

[▽]Jiangsu Key Laboratory of Thin Films, School of Physical Science and Technology, Soochow University, Suzhou 215006, China

Supporting Information

ABSTRACT: To break through a critical barrier in the practical application of graphene biosensors, namely, device-to-device performance inhomogeneity, this work presents a novel scenario employing a fully solid-state (FSS) transistor configuration. Herein, the graphene sensing unit is completely encapsulated by a high-κ solid dielectric material, which isolates the sensing unit from solution contaminants and thus homogeneously maintains the extraordinary carrier mobility of pristine graphene in batch-made devices. To create an interface sensitive to biomolecular interactions based on the FSS configuration, a metallic floating gate functionalized by conductive mercapto-phenyl molecular linkers is defined on the top-layer solid dielectric. As the solid dielectric layer beneath the metal floating gate enables a higher capacitive gating efficiency than the regular graphene-solution electrical double layer (EDL) interface, the overall transistor amplification gain is further enhanced. As a proof of principle, a label-free DNAzymatic bioassay of Pb^{2+} is conducted. Without the traditional one-by-one device normalization, an excellent concentration detection limit of 929.8 fM is achieved, which is almost 2 orders of magnitude lower than that in existing works. The FSS configuration allows enhanced sensitivity and homogeneity, thereby providing new developmental guidelines for graphene biosensors beyond the laboratory investigation stage. Additionally, it has the potential to be universally applicable for cost-efficient single-device bioassays.

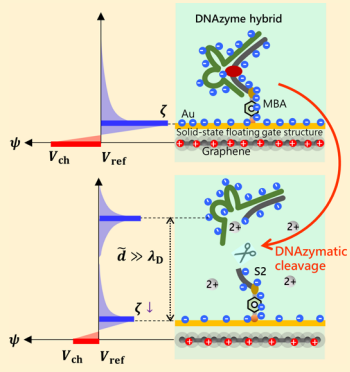

KEYWORDS: *Fully solid-state transistor configuration, practical graphene biosensor, device-to-device homogeneity, DNAzymatic bioassay, subpicomolar Pb^{2+} detection*

Graphene, a monatomic carbon hexagonal crystal, is a semimetal material with the highest carrier mobility ever known,[1] which has allowed the development of advanced electronic sensors.[2] In particular, its superior chemical stability in aqueous media makes graphene an exceptional bioelectronic nanomaterial.[3] On the basis of these advantages, graphene biosensors under the transistor configuration are capable of directly transducing biomolecular interactions into distinct conductivity outputs, thus realizing high-precision label-free analysis with simplified measurement peripherals.[4]

To date, however, the use of graphene field-effect transistor (GFET) biosensors is still limited in the laboratory. The authors attribute the primary hindrance to the performance inhomogeneity of existing GFETs. Although wafer-size graphene synthesis with high homogeneity has been achieved by chemical vapor deposition (CVD),[5] the fundamental principle of current biosensor configurations cannot protect the graphene electrical characteristics from contamination in the surrounding solutions.[6−8] The hydrophobic graphene sensing unit directly open to the aqueous medium is prone to irreversibly adsorbing extrinsic contaminants, which cause the intrinsic mobility to deteriorate and degrade the biosensing performance. To make matters worse, even the batch-made GFETs suffer from random performance degradation, which causes individual devices to have discretely distributed output properties and prevents them from being interchangeable.[9,10] This device-to-device inhomogeneity severely limits the practical implementation of GFET biosensors in single-device biochemical analysis.[11]

Received: August 27, 2019
Revised: December 8, 2019
Published: December 9, 2019

DOI: 10.1021/acs.nanolett.9b03528
Nano Lett. 2020, 20, 166−175

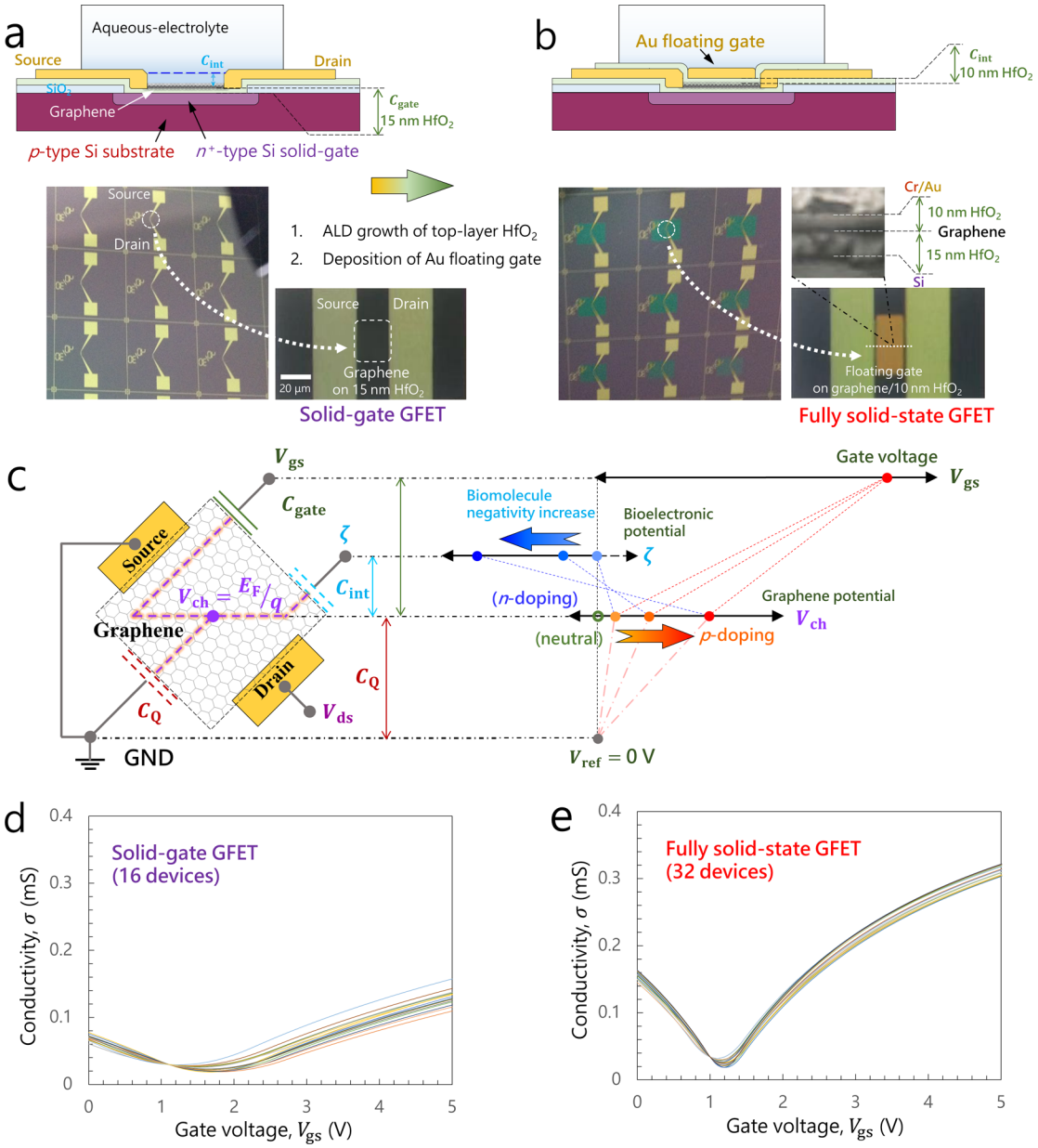

Figure 1. GFET electronic sensor devices, equivalent circuit model, and transfer characterization results. (a,b) Schematics and specimens of previous SG-GFET and newly configured FSS-GFET devices. The optical micrographs in (a,b) show the square graphene sensing unit in FSS- and SG-GFETs with a size of 20 μm × 20 μm. The cross-section SEM image in (b) presents the physical structure of the FSS configuration. (c) Capacitive equivalent circuit model of GFET biosensors. (d,e) Transfer characteristic curves of 16 SG-GFET and 32 FSS-GFET devices before biochemical functionalization. The transfer characteristic measurements were all executed in a HEPES buffer solution (pH ≈ 7.4, ionic strength $I \approx$ 50 mM).

To overcome these limitations, we sought to improve the fundamental principle of GFET configuration. Building upon our previous investigation, which improved the primitive solution-gate GFETs with a stable solid-gate (SG) structure,[10,12−14] this work further develops a fully solid-state (FSS) GFET configuration. Here, a solid dielectric structure with a deposited metal floating gate electrode is implemented for bioelectronic interactions, replacing the conventional graphene-solution interface. As contaminants in the solution are isolated by the solid dielectric top-layer, the encapsulated graphene homogeneously maintains its intrinsic properties. For the FSS configuration, a conductive mercapto-phenyl molecular linker is adopted to immobilize biomolecules on the metal floating gate surface. In contrast to the effect of the widely used nonconductive alkyl molecular linker, the bioelectronic charges are efficiently conducted onto the floating gate. Compared with the graphene-solution electrical double layer (EDL), the solid-state dielectric structure has a higher capacitive gating efficiency, which significantly enhances the sensitivity to biomolecular interactions. By verification using a DNAzymatic Pb^{2+} bioassay,[15] which involves a well-established biomolecular interaction mechanism, we achieve a subpicomolar ($<10^{-12}$ M) concentration detection limit of Pb^{2+}, almost 2 orders of magnitude lower than those obtained in previous similar works.[16,17] This excellent performance achieved by the FSS configuration supplies a developmental guide for label-free GFET biosensors, as researchers are pursuing highly

DOI: 10.1021/acs.nanolett.9b03528
Nano Lett. 2020, 20, 166−175

homogeneous GFETs to obtain practicable single-device electronic bioassays with interchangeable devices.

Results and Discussion. *Sensor Device.* As mentioned above, the FSS-GFET sensor was designed based on our previous SG-GFET devices.[10,12−14] The batch tape-out of devices (48 devices per wafer) was made using standard IC fabrication techniques. The detailed protocol is provided in Supporting Information (SI) Figure S1. In brief, as shown in the schematic of SG-GFET in Figure 1a, the graphene sensing unit ($W = L = 20\ \mu m$) stretching over the drain and source electrodes was gated by a local planar electrode through a 15 nm HfO_2 dielectric layer, which was fabricated by atomic layer deposition (ALD). In pursuit of ideal graphene quality, we chose the oxygen-assisted CVD-grown graphene with large-area monolayer single crystals.[5] In particular, to reduce the effects of roughness and disorder on the graphene,[18] the local back-gate electrode was directly made by employing localized complementary ion implantation (phosphorus ions) in the p-type silicon wafer substrate instead of the previous approach using a metal-deposited gate electrode.[19] Therefore, the voltage of the p-type substrate was lower than that of the heavy n^+-type Si gate electrode in order to avoid substrate leakage current with the reverse biased p−n junction. After the fabrication of the SG-GFETs, 16 devices were diced from the wafer for use in subsequent control experiments, and the remaining 32 devices were further fabricated into FSS-GFETs (Figure 1b). As shown in the scanning electron microscopic (SEM) image in Figure 1b, the graphene sensing unit was encapsulated by a 10 nm HfO_2 top-layer locally grown via ALD followed by overlying Cr/Au floating gate electrode deposition to complete the FSS-GFET device fabrication. By further biochemical functionalization (Figure S2 in SI), the GFET devices can be modified into electronic biosensors. In particular, to ensure the high-quality growth of the HfO_2 layer on the graphene surface, avoiding pinhole and peeling-off risks, we utilized ozone (O_3) as the ALD oxidant in this work[20,21] instead of the more widely used water vapor. By means of the O_3-created oxygenic groups and bonds, the shortcoming of graphene lacking dangling bonds for hafnium precursor absorption[22−24] can be overcome. The stable absorption of hafnium precursor molecules may thus be used to ensure the reliability of our batch-made devices.[25−27]

On the basis of the schematics in Figure 1a,b, we extracted the universal equivalent circuit model of GFET biosensors. As shown in Figure 1c, our FSS- and SG-GFET devices can be both described by a dual-gate capacitive network.[28] While the back-gate electrode applies a voltage V_{gs} via the parallel-plate back-gate capacitance C_{gate} (15 nm HfO_2), the biomolecular charges in the vicinity of the graphene surface concurrently apply an excitation ζ via the interfacial effective capacitance C_{int}.[29] By taking the graphene quantum capacitance C_Q into account,[30] V_{gs} and ζ impact the chemical potential V_{ch} of the graphene sensing unit under the constraint of the capacitive network. The variation in V_{ch}, as well as the fluctuation in the graphene Fermi energy level E_F, is related to the graphene carrier density n by $qV_{ch} = E_F = \hbar v_F \sqrt{\pi n}$.[31] Considering the classic Drude model of graphene conductivity $\sigma = q\mu n$,[32] the directly measurable GFET conductivity $\sigma = I_{ds}/V_{ds}$, which is proportional to the carrier density, can reflect the common impacts of bioelectronic excitations.

As explained by the capacitive model in Figure 1c, the bioelectronic excitations can be measured as the variation in GFET conductivity σ at fixed drain voltage V_{ds} and gate voltage V_{gs}. A certain biomolecular interaction may lead to different conductivity responses in the SG- and FSS-GFET biosensors due to the difference in configuration.[33] Prior to the biosensing verification, we characterized the electronic performances of our GFET devices, such as the amplification capability and device-to-device homogeneity. We used a semiconductor analyzer to measure the GFET transfer characteristics with respect to the gate voltage scanning (σ vs V_{gs}).[34] To ensure experimental consistency in this work, all the measurements were executed in the same 4-(2-hydroxyethyl)-1-piperazineethanesulfonic acid (HEPES) buffer solution (prepared by dissolving 50 mM HEPES and 50 mM $NaNO_3$ in Milli-Q deionized water, pH ≈ 7.4, ionic strength $I \approx 50$ mM). We considered that the transfer characteristic curves of GFETs usually exhibit dependence in the gate voltage scanning conditions, such as the V_{gs} scanning direction and velocity, due to the hysteresis effect.[35] To define suitable measurement conditions to reduce the hysteresis effects, we first executed a systematic hysteresis characterization (see Figures S3−S8 in SI for details). We discovered that the transfer characteristics of FSS-GFETs are stable in the range of $V_{gs} \in [0\ V, 5\ V]$ and almost irrelevant to the scanning direction and velocity (Figures S3−S5 in SI). This phenomenon could be attributed to the unique p−n junction gate structure that allows only unipolar scanning with positive gate voltages. In other words, electrons rapidly fill the traps in the back-gate HfO_2 layer during the unipolar V_{gs} scanning and persist in saturation (negative V_{gs} compensating holes not allowed). This interpretation supports the unrecognizable hysteresis observation and is in agreement with our previous findings.[36] Therefore, the irreversibly trapped electrons reduced the hysteresis-led measurement uncertainties and are beneficial for the discussion of device performance. Although the non-neutralizable electrons redundantly strengthen the p-type doping of graphene and may lead to overestimation of the values of bioelectronic signals, our biosensors typically focus on the relative output variations instead of absolute values that may still maintain unchanged device parameters, such as sensitivity and resolution. In contrast, the transfer characteristic curves of SG-GFETs exhibit a relatively high dependence on the V_{gs} scanning conditions (Figures S6−S8 in SI). This phenomenon can be attributed to the EDL electrochemical hysteresis without the top-layer solid dielectric insulation. That means for SG-GFETs the redistribution and equilibrium of ambient ions on the graphene−solution interface may exhibit a resonance frequency, which requires the proper V_{gs} scanning velocity to reduce hysteresis effects.[37] On the basis of the hysteresis characterization results, we chose forward V_{gs} scanning with a velocity $v = 1\ V\ s^{-1}$, which provides relatively stable transfer characteristics for the SG-GFETs and minimizes hysteresis errors. Because the scanning condition for FSS-GFETs is not strictly required, forward V_{gs} scanning with a velocity $v = 1\ V\ s^{-1}$ was consistently used in this work to guarantee the reliable comparability of the transfer characteristic curves.

Under the well-defined measurement condition, the transfer characteristic curves of FSS- and SG-GFETs were measured as shown in Figure 1d,e, respectively. Compared with SG-GFETs, FSS-GFETs show much better similarity in transfer characteristic curves, and the device-to-device homogeneity is comparable to that of commercial silicon transistors. Considering that two kinds of devices possess the same back-gate capacitance C_{gate}, and the absence of bioelectronic

DOI: 10.1021/acs.nanolett.9b03528
Nano Lett. 2020, 20, 166−175

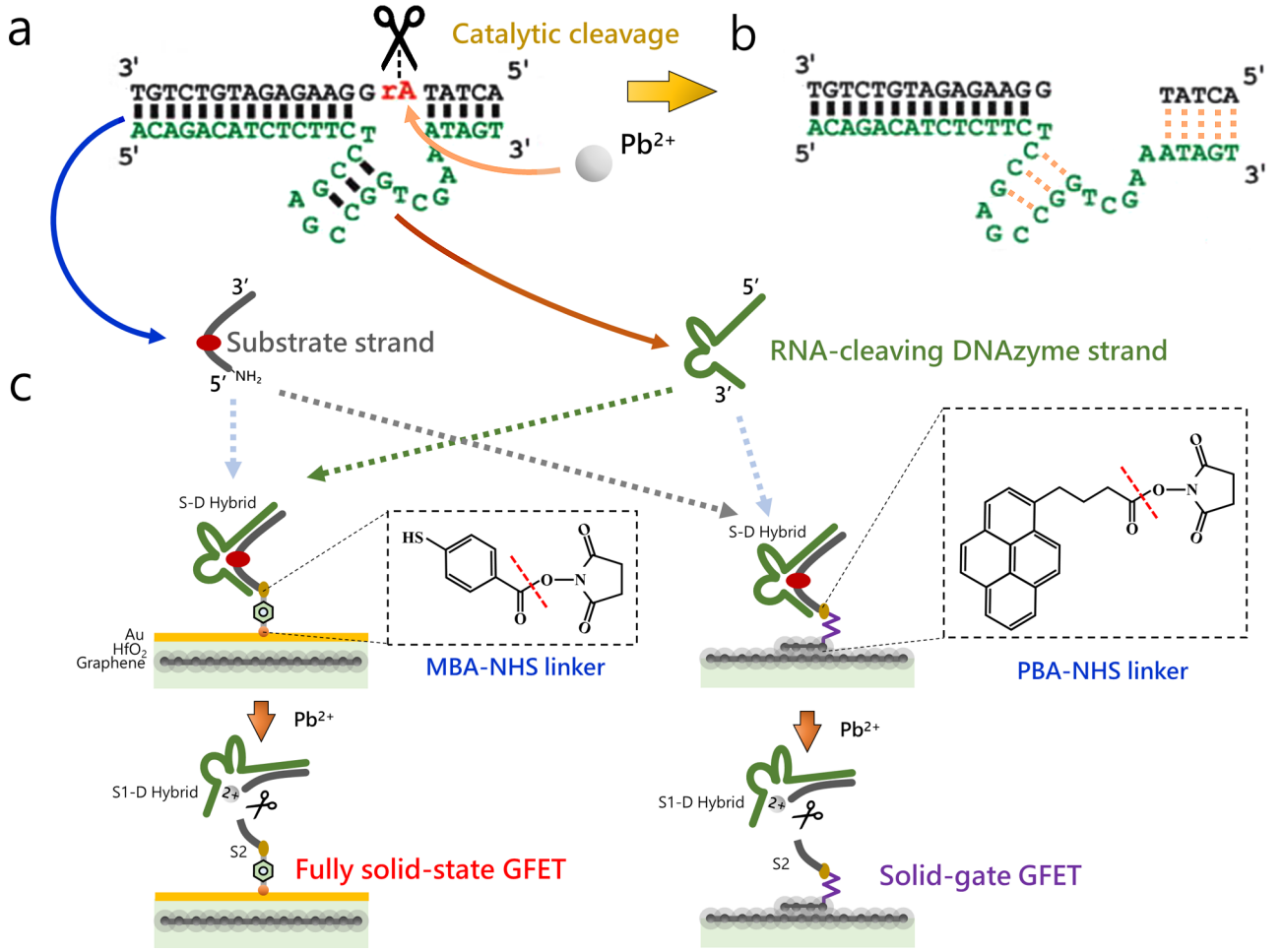

Figure 2. Biosensing principle of the DNAzymatic analysis of Pb^{2+}. (a) Complementarily hybridized DNAzyme and substrate strands. (b) Pb^{2+}-catalyzed cleavage at the RNA base site. (c) Biochemical functionalization schemes and biomolecular interaction designs of the DNAzymatic Pb^{2+} analysis for FSS- and SG-GFET devices.

excitation in these tests minimizes the impact of interfacial capacitance C_{int}, the only reasonable explanation for the improvement in homogeneity is the protection of graphene carrier mobility μ, owing to the FSS encapsulation. The contaminants in solution reversibly adsorb and desorb on the hydrophilic metal floating gate surface and are reliably isolated from the graphene sensing unit.[6−8] Moreover, we also discovered that the FSS-GFET transfer characteristic curves (Figure 1e) are collectively steeper than those of the SG-GFETs (Figure 1d). The increase in the transfer characteristic curve slope (transconductance amplification gain g_m) can also be attributed to the reduction in contaminants, which preserves the pristine graphene mobility.[38] As the enhancement in g_m indicates larger amplification capability and higher sensitivity,[39,40] the FSS-GFET biosensors may possess greater quantitation capability combined with improved homogeneity.

DNAzymatic Analysis Principle. After the device characterization, we designed a DNAzymatic analysis of the Pb^{2+} bioassay to demonstrate the advantages of the novel FSS-GFET devices. Because the Pb^{2+}-specific DNAzyme has been thoroughly investigated,[16,41] the reliable biomolecular interaction mechanism is able to provide solid evidence for the biosensing performance discussion. As shown in Figure 2, the 8−17 DNAzyme sequence (5′−ACA GAC ATC TCT TCT CCG AGC CGG TCG AAA TAG T−3′) was employed for its affinity to Pb^{2+} ions. An amino group-modified single strand (5′−NH_2−ACT ATrA GGA AGA GAT GTC TGT−3′) was customized as the complementary substrate based on the 17DS-5 sequence.[15] When a Pb^{2+} ion is present at the binding site of DNAzyme (Figure 2a), the pistol-like conformation enables the catalytic RNA-adenine site hydrolyzation and cleaves the substrate strand (Figure 2b).[42] Considering that the oligonucleotide strands in aqueous medium are electrically charged conductors,[43,44] the Pb^{2+}-dependent catalytic cleavage is capable of bioelectronic signaling via an electric field-effect. To graft the DNAzymatic analysis principle into our FSS-GFET biosensors, the hybrid of the substrate and DNAzyme strands (denoted S−D) was immobilized in the vicinity of the graphene sensing unit surface (Figure 2c). A thiol-group linker,[45] mercaptobenzoic acid *N*-hydroxysuccinimide ester (MBA-NHS), was used to immobilize the S−D hybrid molecule on the gold floating gate.[46] The S−D hybridization without RNA cleavage is almost irreversible at room temperature because of the high melting temperature of helix strands ($T_m \approx 52$ °C).[47] While a Pb^{2+} ion cleaves the RNA-adenine site, the 5-mer hybridization supplied by the remnant substrate strand (denoted S2 in Figure 2c) is much weaker ($T_m \approx 12$ °C) and thus prone to spontaneously release of the remaining part of the hybrid (denoted S1−D) away from the graphene sensing unit.[48] Consequently, the electric field-effect intensity applied by the charges of the oligonucleotide strands is related to the catalytic cleavage progress. In addition, the

DOI: 10.1021/acs.nanolett.9b03528
Nano Lett. 2020, 20, 166−175

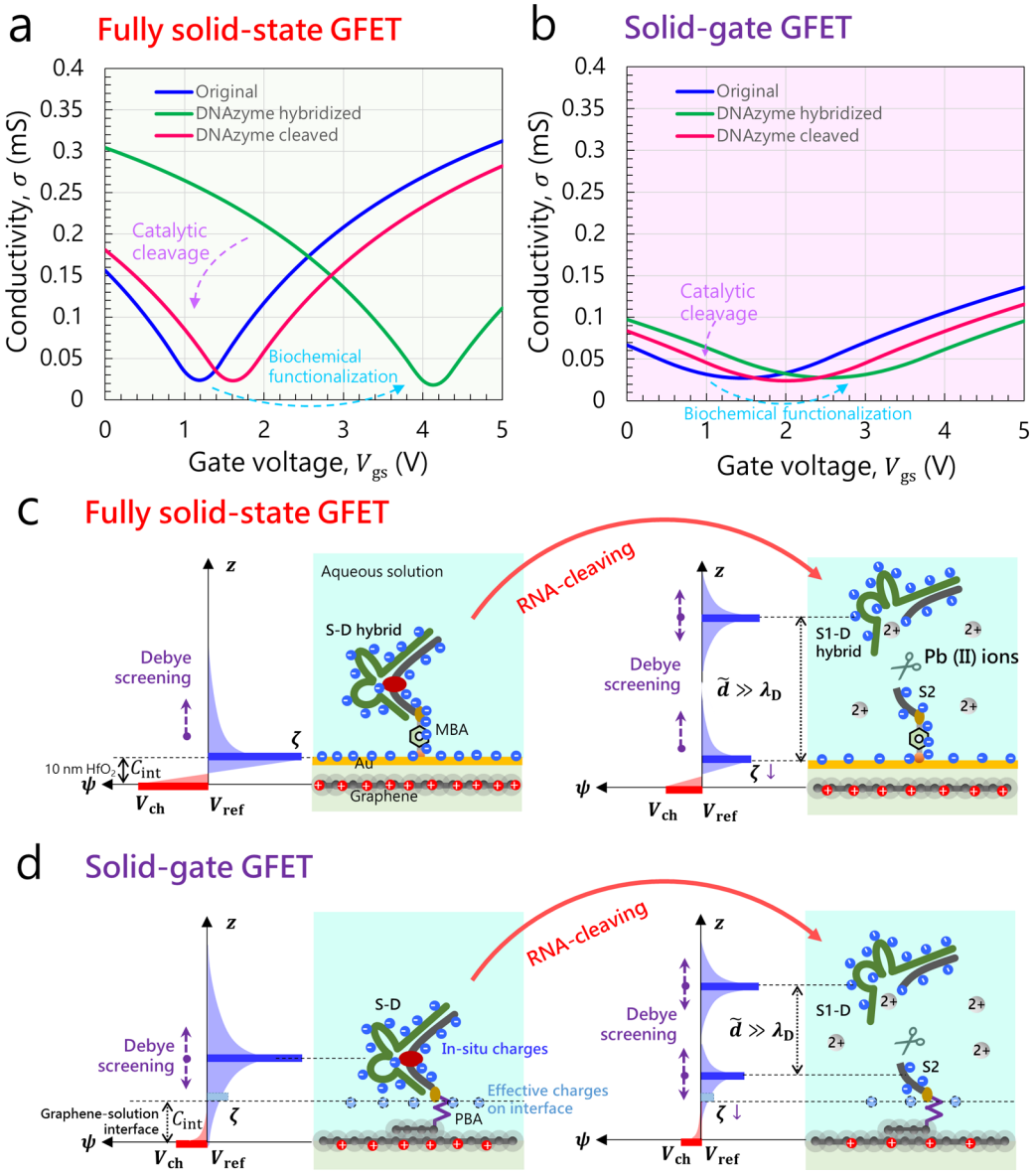

Figure 3. Changes in GFET transfer characteristics with respect to DNAzymatic Pb^{2+} analysis. (a,b) Transfer characteristic curves of representative FSS- and SG-GFET devices. The red curves in (a,b), corresponding to the final state of complete cleavage, are acquired from the devices after the kinetic detection of Pb^{2+} ions (see kinetic observation experiments in the next section). (c,d) Electric field-effect signaling mechanisms of FSS- and SG-GFET biosensors. For FSS-GFETs (c), the molecular linker is a conductive mercapto-phenyl linker MBA-NHS, by which bioelectronic charges are transferred to the gold floating gate electrode to apply an electric field-effect. For SG-GFETs using conventional nonconductive alkyl linker PBA-NHS (d), the electric field-effect is applied by in situ distributed charges via the effective EDL in aqueous solution.

Pb^{2+} concentration, which determines the cleavage rate, could be kinetically detected by observing the ratio of DNAzymatic analysis.[49]

Based on the DNAzymatic analysis principle designed in Figure 2c, we functionalized 24 FSS-GFET devices for the Pb^{2+} biosensing experiments (see Figure S2 in SI for detailed protocol). On the other hand, 16 SG-GFET devices were functionalized for the control experiments comparing the device performance. We executed the same functionalization method on SG-GFETs but used the conventional 1-pyrenebutyric acid *N*-hydroxysuccinimide ester (PBA-NHS) as the $\pi-\pi$ stacking molecular linker[14] instead of MBA-NHS.

Bioelectronic Signaling Characterization. We then characterized the bioelectronic signaling capability of 24 FSS-GFETs and 16 SG-GFETs based on the DNAzymatic analysis principle (see Figures S9 and S10 in SI for the complete data set). As shown in Figure 3a,b, the lateral shifts in the representative transport characteristic (σ vs V_{gs}) curves illustrate the signaling in both GFET devices. By referring to the equivalent circuit describing the bioelectronic signaling mechanism (Figure 1c), while the oligonucleotide S−D hybrid molecules introduce negative charges on the biointerface, the graphene sensing unit exhibits opposite p-type doping, arising from the electric field-induced holes (green curves in Figure 3a,b). After catalytic cleavage, the partial S1−D hybrid molecules are released into the bulk solution. As the Debye screening length in the buffer solution with the ionic strength $I \approx 50$ mM is calculated as $\lambda_D \approx 1.378$ nm,[14] the released S1−D hybrid molecules are much farther in mean distance from the sensitive interface ($\tilde{d} \gg \lambda_D$ in Figure 3c,d); thus, the electric

DOI: 10.1021/acs.nanolett.9b03528
Nano Lett. 2020, 20, 166−175

field-effect is negligible.[50] In other words, the interfacial accumulation of negative charges from the remnant S2 strands is much lower, and the p-type doping of the graphene sensing unit is correspondingly compromised (red curves in Figure 3a,b). The complete experimental results are shown in SI Figures S9 and S10, and all the FSS- and SG-GFET devices exhibit the same evolutionary trend in the transfer characteristic curve shifts, specifically a right shift followed by a left shift, which is in agreement with our theoretical expectation.

Meanwhile, we discovered that the FSS-GFETs homogeneously maintained the steep transfer characteristic curves with a higher transconductance amplification gain than that of the SG-GFETs, while the biomolecular interactions were incorporated (see Figure S9 and S10 in SI for comparisons). The homogeneity and sensitivity advantages could also be attributed to the isolation of contaminants resulting from the FSS configuration. Consequently, by fixing the gate voltage at an appropriately chosen value, the well-protected FSS-GFET biosensors are capable of an output conductivity response with higher amplification gain and accuracy with respect to a certain lateral shift.

Moreover, there is one more attractive phenomenon illustrated in Figure 3a,b: at properly chosen gate voltages (e.g., V_{gs} = 1.5 V for FSS-GFETs and V_{gs} = 1 V for SG-GFETs), the same catalytic cleavage renders the conductivity response of FSS-GFETs almost 10 times larger in amplitude than that of SG-GFETs. Since the transconductance enhancement obtained from the mobility protection of the FSS configuration is only several times, we attribute the greater conductivity output to the larger lateral shift in the transfer characteristic curves in Figure 3a. Therefore, on the basis of the Drude model $\sigma = q\mu n$, it is strongly implied that the variation in carrier density n arising from a certain bioelectronic excitation is also strengthened under the FSS configuration. For a theoretical elucidation, it is imperative to return to the equivalent circuit of GFET biosensors in Figure 1c, in which the capacitive network describes the signaling mechanism, corresponding to the difference in configuration between FSS- and SG-GFETs.

As shown in Figure 1c, the chemical potential of the graphene sensing unit $V_{ch} = E_F/q$ is constrained by the capacitive network (E_F is the Fermi energy level). Because of the finite density of state (DOS) of graphene energy bands, the quantum capacitance of graphene C_Q is also finite.[28,30] Therefore, the graphene potential V_{ch} fluctuates with respect to the control of back-gate voltage V_{gs} via the capacitances in series $C_{gate}C_Q/(C_{gate} + C_Q)$ and with respect to the impact of effective interfacial bioelectronic potential ζ via $C_{int}C_Q/(C_{int} + C_Q)$. This electrical relation is described by the charge conservation law as follows

$$V_{ch}C_Q - \left(V_{gs}\frac{C_{gate}C_Q}{C_{gate} + C_Q} + \zeta\frac{C_{int}C_Q}{C_{int} + C_Q}\right) = q(n_0 + n_{gate} + n_{bio}) \quad (1)$$

On the left side of eq 1, the first item is the accumulated charge density on graphene corresponding to the potential V_{ch} applied on C_Q in which graphene is the upper plate of C_Q. The second item in brackets expresses the algebraic sum of the charge density on graphene induced by the V_{gs} and ζ charging via C_{gate} and C_{int}, in which graphene is the bottom plate of C_{gate} and C_{int}. On the right side, the overall charge density $q(n_0 + n_{gate} + n_{bio}) = qn$ consists of the constant carriers from impurities n_0, gate voltage adjustment n_{gate}, and bioelectronic potential impact n_{bio}. In eq 1, the quantum capacitance C_Q has a complicated functional expression[28,30]

$$C_Q = \frac{2q^2k_BT}{(\pi\hbar^2v_F^2)}\ln\left[2\left(1 + \cosh\frac{qV_{ch}}{k_BT}\right)\right] \quad (2)$$

However, while the intrinsic impurity excitation n_0 at room temperature (T = 300 K) ensures $qV_{ch} \gg k_BT$, eq 2 can be reduced to the simplified form $C_Q \approx 2q^2\sqrt{n}/(\hbar v_F\sqrt{\pi})$[28,30] by introducing the graphene band structure relation $qV_{ch} = \hbar v_F\sqrt{\pi n}$ mentioned above.[31] Since typically $n_0 \geq 10^{12}$ cm^{-2} and $n > n_0$, C_Q is at the level of approximately 10 μF cm^{-2}, much larger than C_{gate} and C_{int}. Thereby, eq 1 can be approximated as follows

$$2qn - (V_{gs}C_{gate} + \zeta C_{int}) = qn \quad (3)$$

Importantly, eq 3 presents a direct constraint relation between the gate voltage adjustment and the bioelectronic excitation, which maintain the graphene carrier equilibrium together. In other words, while the graphene carrier density n remains constant during a bioelectronic interaction, the gate voltage adjustment supplies corresponding charge compensation identical to the variation in bioelectronic charges. Therefore, we choose the minimal conductivity points (at $V_{gs} = V_{Dirac}$) as identifiers to quantitatively discuss the lateral shifts in the GFET transfer characteristic curves. The green and red curves of a representative FSS-GFET device are shown in Figure 3a, and the left shift of Dirac point $\Delta V_{Dirac} \approx 2.53$ V, with respect to the DNAzymatic cleavage, reflects the decrease in holes in graphene with a density $\Delta n = \Delta V_{Dirac}C_{gate}/q \approx 1.493 \times 10^{13}$ cm^{-2}. Correspondingly, the electron density decrease on the gold floating gate is also 1.493×10^{13} cm^{-2}. Since a 55-mer S−D hybrid molecule brings 55 electrons via phosphodiester group ionization, and the catalytic cleavage results in the loss of 50 electrons per molecule, the total electron loss per unit area is estimated to be 5×10^{13} cm^{-2}, based on the typical value of DNA immobilization density ($\sim 10^{12}$ cm^{-2}) on a gold surface.[51−53] The estimation above presents a reasonable signaling mechanism, as shown in Figure 3c. Since the phenyl linker contains π-bonds and is electrically conductive,[54] a portion of the electrons (1.493/5 ≈ 30%) from the anchored biomolecules can pass through MBA linkers onto the gold floating gate (Figure 3c)[55] and apply an electric field-effect via the top-layer solid capacitance. The comparatively smaller change in gate surface electron density with respect to the DNAzymatic cleavage (1.493×10^{13} cm^{-2} < 5×10^{13} cm^{-2}) suggests a relatively high gating efficiency of the FSS configuration in biomolecular interactions.

In contrast, for the conventional SG-GFET device with the same DNAzymatic cleavage, the Dirac point shift is much smaller $\Delta V_{Dirac} \approx 0.63$ V (Figure 3b). As the SG-GFETs possess a back-gate structure same as to that of the FSS-GFETs, the corresponding hole density decrease in graphene $\Delta n \approx 3.718 \times 10^{12}$ cm^{-2} suggests a lower gating efficiency of the graphene−solution interface. This result can be attributed to the Debye screening effect, as shown in Figure 3d. As the alkyl molecule consisting of σ-bonds is electrically nonconductive, the electrons on the PBA-anchored molecules apply an electric field-effect in situ via EDL. Following the Debye−Hückel theory, the HEPES buffer solution exponentially reduces the effective electron density on the graphene−

DOI: 10.1021/acs.nanolett.9b03528
Nano Lett. 2020, 20, 166−175

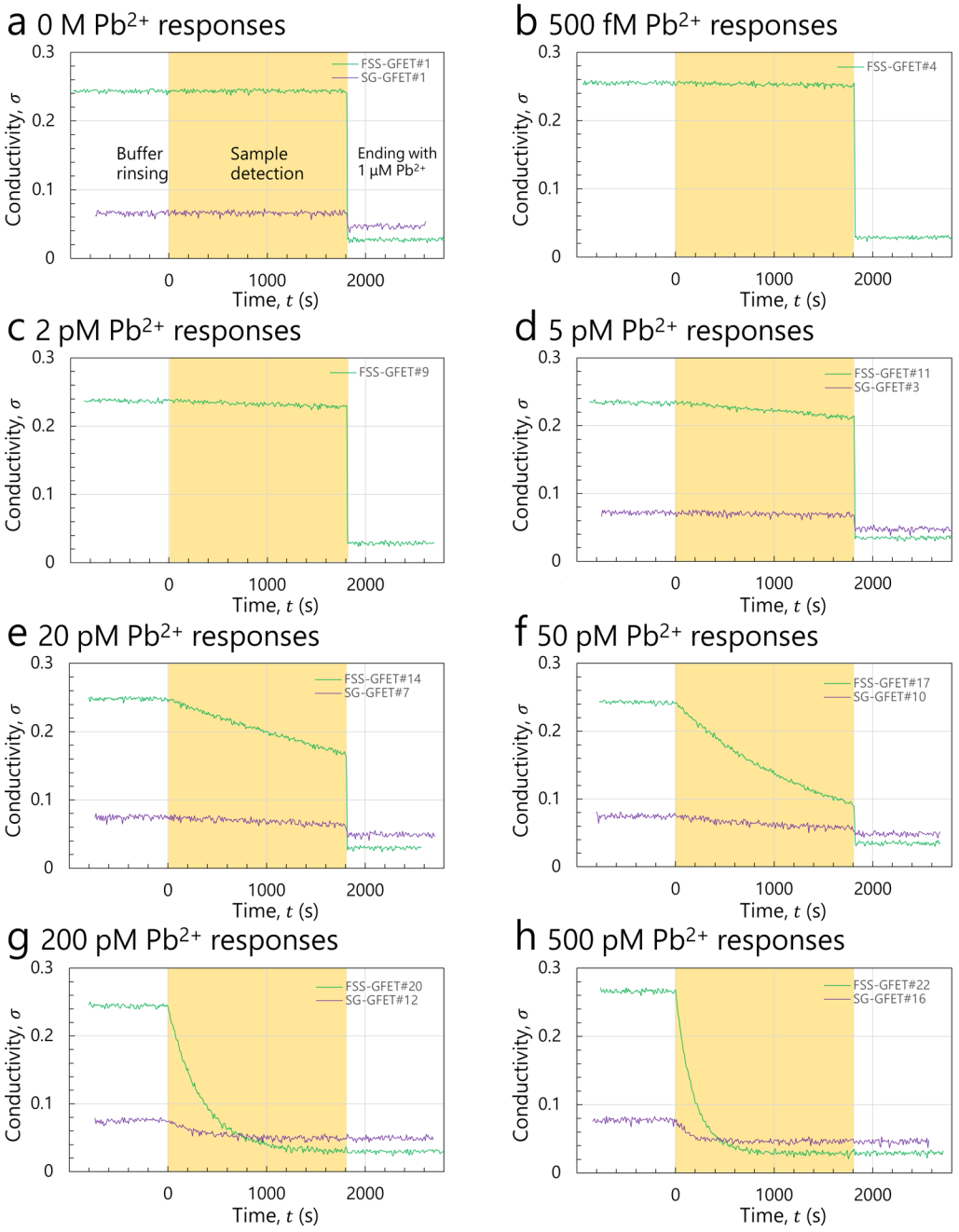

Figure 4. Representative kinetic processes of various Pb^{2+} samples observed by FSS- and SG-GFET devices. (a) c = 0 M. (b) c = 500 fM. (c) c = 2 pM. (d) c = 5 pM. (e) c = 20 pM. (f) c = 50 pM. (g) c = 200 pM. (h) c = 500 pM. FSS-GFET devices clearly exhibit more powerful Pb^{2+} quantitation capabilities than SG-GFET devices.

solution interface, thereby leading to a lower gating efficiency than that of the FSS configuration.

To further support our explanation, additional control experiments were performed. As shown in SI Figure S2c,d, we employed 3-mercaptopropionic acid *N*-hydroxysuccinimide ester (MPA-NHS) and mercaptododecanoic acid *N*-hydroxysuccinimide ester (MDA-NHS) to functionalize 4 FSS-GFET devices, respectively. As shown in SI Figure S11, the nonconductive MPA linker with the size similar to those of MBA and PBA (~1.3 nm) brings the lateral shift amplitude of the FSS-GFET transfer characteristic curves close to that of SG-GFETs, although the transconductance advantage remains unchanged. In addition, when the linker is nonconductive MDA (SI Figure S12), the molecule size, which is much longer than the Debye screening length in buffer solution, almost disables the bioelectronic signaling capability. Altogether, these control experiments support the elucidation of the performance improvement of FSS-GFET biosensors, which is attributed to the graphene mobility protection and bioelectronic gating efficiency enhancement.

Target Analyte Detections. As the bioelectronic signaling mechanism clarified, the Pb^{2+} bioassay was carried out to test the biosensing performance, especially the performance improvement of our FSS-GFET devices. By using 24 FSS-GFETs, we detected Pb^{2+} samples at 8 concentrations (0 M, 500 fM, 2 pM, 5 pM, 20 pM, 50 pM, 200 pM, and 500 pM, all

DOI: 10.1021/acs.nanolett.9b03528
Nano Lett. 2020, 20, 166−175

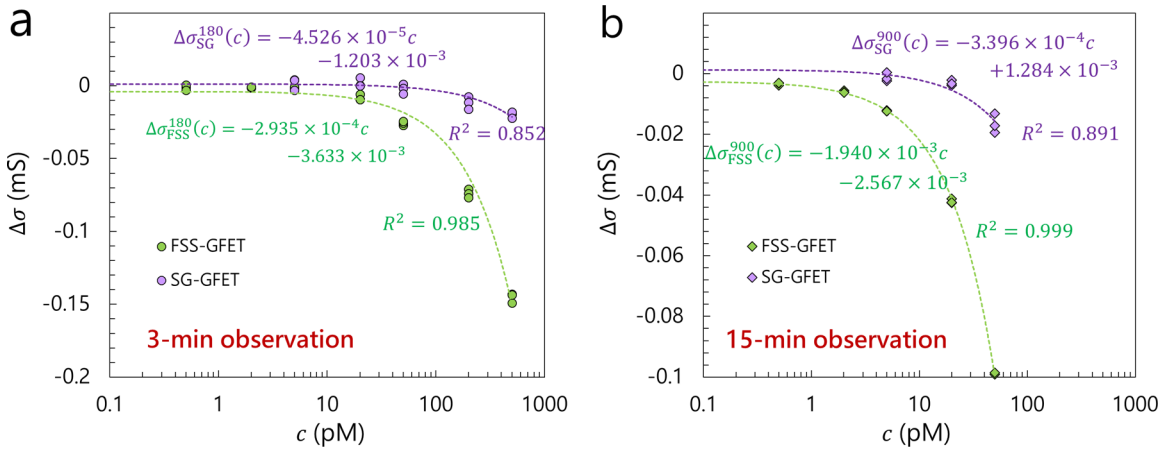

Figure 5. FSS- and SG-GFET conductivity responses of Pb^{2+} samples at various concentrations. (a) For the detection of Pb^{2+} concentration, the 180 s observations allow detection covering the entire concentration range 0−500 pM. However, the 180 s responses of high-concentration samples contain systematic errors due to kinetic saturation nonlinearity. (b) For the detection of more diluted Pb^{2+} samples within the concentration range of 0−50 pM, the saturation errors are negligible. The prolonged 900 s observations fully exploit the biosensing capability of GFET devices. In particular, the linear calibration curve of FSS-GFETs with perfect regression (R^2 = 0.999) clearly illustrates that the performance advantage benefited from the enhanced device-to-device homogeneity and sensitivity.

prepared in HEPES buffer). The sample detection at each concentration was measured in triplicate, and each measurement used a disposable device. During experiments, the Pb^{2+} samples were syringed into sensor devices by a microfluidic system, and the FSS-GFET conductivity responses were continuously recorded over time as kinetic processes (σ vs t) under the control of a fixed gate voltage V_{gs} = 1.5 V. In addition, 16 SG-GFETs were used to detect Pb^{2+} samples at 6 concentrations (5, 20, 50, 200, and 500 pM). The kinetic conductivity observations of SG-GFET biosensors were carried out at V_{gs} = 1 V.

The complete experimental results of 40 devices are provided in the data set SI Figures S13 and S14. In Figure 4, the representative results selected from the data set are plotted as kinetic processes to display the sensing performances. Because the catalytic cleavage in the presence of Pb^{2+} ions has an exponential trend, the Pb^{2+}-accelerated cleavage rate, as well as the saturation rate of kinetic processes, can be exploited to quantify the Pb^{2+} concentration. As shown in Figure 4, the positive acceleration corresponding to the increase in Pb^{2+} concentration is illustrated by both the FSS- and SG-GFETs. We learned that the responses from FSS- and SG-GFET biosensors are both proportionally related to the concentration of Pb^{2+}. However, the larger dynamic range of FSS-GFETs, as shown in Figure 3, supplies greater conductivity responses than SG-GFETs under a certain amperometric noise level. Consequently, the FSS-GFET biosensors possess a more powerful quantification capability for diluted samples.

On the basis of the kinetic observations, we calibrated the quantitative relationship between sensor response and Pb^{2+} concentration. According to the biomolecular affinity theory, the exponential kinetic process supplies an approximate linear short-time response relating to the analyte concentration.[10] Therefore, to prevent kinetic process saturation errors, the conductivity variations in FSS- and SG-GFETs observed at t = 180 s are plotted in the Pb^{2+} concentration range 0−500 pM (Figure 5a). In particular, to verify the device-to-device homogeneity of our FSS-GFETs in biosensing, the conductivity variation of each device $\Delta\sigma$ is directly used as the sensor response ($R(t) = \sigma(t) - \overline{\sigma}_{t<0} = \Delta\sigma$) to describe the concentration dependence ($\Delta\sigma$ vs c) instead of the normalized interaction ratio ($R(t) = (\sigma(t) - \overline{\sigma}_{t<0})/(\overline{\sigma}_{t>1800} - \overline{\sigma}_{t<0})$), which has been widely adopted in previous investigations.

As shown in Figure 5a, the 180 s responses of FSS- and SG-GFETs are extracted from the kinetic processes (see Figures S13 and S14 in SI) and plotted versus the Pb^{2+} concentrations (0−500 pM). The linear calibration curve of FSS-GFETs possesses the 180 s response sensitivity $S_{FSS}^{180} = -2.935 \times 10^{-4}$ mS pM^{-1} and standard deviation $\chi_{FSS}^{180} = 6.080 \times 10^{-3}$ mS (see statistical results in SI Tables S1 and S2). Thus, the limit of detection (LOD) of Pb^{2+} concentration is estimated as[56] $LOD_{FSS}^{180} = 3|\chi_{FSS}^{180}/S_{FSS}^{180}| = 62.148$ pM. In comparison, the biosensing performance of SG-GFETs is worse than that of FSS-GFETs. As shown in Figure 5a, the linear calibration sensitivity $S_{SG}^{180} = -4.526 \times 10^{-5}$ mS pM^{-1} and standard deviation $\chi_{SG}^{180} = 3.581 \times 10^{-3}$ mS estimate the detection limit as $LOD_{SG}^{180} = 3|\chi_{SG}^{180}/S_{SG}^{180}| = 237.341$ pM. However, we still discovered saturation errors in the 180 s responses of relatively high-concentration Pb^{2+} samples (e.g., 50 and 200 pM symbols in Figure 5a). To minimize the nonlinear saturation influences, we further examined the prolonged 900 s responses of more diluted samples to accurately estimate the performance of our novel FSS-GFET biosensors.

The kinetic processes in SI Figures S13 and S14 reveal that the diluted Pb^{2+} samples within the concentration range 0−50 pM are appropriate for the 900 s observation unaffected by nonlinear saturation errors. As shown in Figure 5b, the linear calibration curve of FSS-GFETs exhibits a sensitivity of $S_{FSS}^{900} = -1.940 \times 10^{-3}$ mS pM^{-1} and a standard deviation of $\chi_{FSS}^{900} = 6.012 \times 10^{-4}$ mS. Hence, the LOD is significantly improved as $LOD_{FSS}^{900} = 3|\chi_{FSS}^{900}/S_{FSS}^{900}| \approx 929.8$ fM. In comparison, the sensitivity and standard deviation of SG-GFETs are $S_{SG}^{900} = -3.396 \times 10^{-4}$ mS pM^{-1} and $\chi_{SG}^{900} = 2.413 \times 10^{-3}$ mS, which only render the LOD of SG-GFETs as $LOD_{SG}^{900} = 3|\chi_{SG}^{900}/S_{SG}^{900}| \approx 21.320$ pM.

On the basis of the experimental and statistical results, we summarize the merits of our FSS-GFET devices as follows. First, the FSS-GFETs offer better sensitivity than conventional SG-GFETs, as confirmed by the calibration curves with enhanced slope values (Figure 5). The better regression

DOI: 10.1021/acs.nanolett.9b03528
Nano Lett. 2020, 20, 166−175

coefficient values (R^2) also demonstrate the improved homogeneity of FSS-GFETs. In addition, we discover that the 180 s responses of FSS-GFETs deviating from the calibration curve in Figure 5a are centered around the high-concentration range, which is attributed to the systematic errors from saturation. Thus, by eliminating the nonlinear saturation influences, as shown in Figure 5b, the FSS-GFET configuration demonstrate a greatly improved homogeneity, improving the LOD to the subpicomolar level without further noise canceling. To our knowledge, the 929.8 fM LOD level (about 192.7 pg L^{-1}) represents the best performance in disposable device-based Pb^{2+} detection, even comparable to that of commercial instrumental methods.

In conclusion, we presented a newly configured FSS-GFET biosensor. By fully encapsulating the graphene sensing unit with a solid dielectric structure, the GFET amplification gain is homogeneously enhanced owing to the elimination of contamination and carrier mobility deterioration. The conduction of bioelectronic signals onto the metal floating gate via phenyl linkers further improves the overall sensitivity. On the basis of the DNAzymatic Pb^{2+} bioassay as a proof of principle, the advantage of our FSS-GFET biosensors is verified via the unprecedented concentration detection limit breaking through the picomole level. More importantly, the FSS-GFET configuration provides excellent homogeneity in batch-made devices, which may open up an opportunity for the practical use of label-free GFET biosensors as disposable devices. As a result, the universal application of a cost-efficient single-device bioassay without reliance on sophisticated instruments might become practical in the future.

■ ASSOCIATED CONTENT

Supporting Information

The Supporting Information is available free of charge at https://pubs.acs.org/doi/10.1021/acs.nanolett.9b03528.

Details of device fabrication and biochemical functionalization, complete data set (PDF)

■ AUTHOR INFORMATION

Corresponding Authors

*E-mail: cwang@tjnu.edu.cn.
*E-mail: yjia2218@seu.edu.cn.
*E-mail: wxye@suda.edu.cn.

ORCID

Yibo Zhu: 0000-0003-4323-1290
Weixiang Ye: 0000-0002-4621-785X

Author Contributions

W.Y. and C.W. conceived the project. Y.J. and C.W. sponsored the research. C.W., J.W., Y.H., Z.S., S.S., and Y.Z. executed the experiments. C.W., Y.J., and W.Y. analyzed the data and provided advice on the project.

Notes

The authors declare no competing financial interest.

■ ACKNOWLEDGMENTS

This work is funded by the Natural Science Foundation of China (61901300), the Natural Science Foundation of Jiangsu Province (BK20180384), the Natural Science Foundation of Tianjin Municipality (18JCYBJC86000), and the Science & Technology Development Fund of Tianjin Education Commission for Higher Education (2018KJ153). C.W. acknowledges the Distinguished Young Talent Recruitment Plan of Tianjin Normal University (011/5RL153) and the Funding Program of the Tianjin Higher Education Creative Team. J.W., Y.H., Z.S., and S.S. acknowledge the Undergraduate Entrepreneurial Creativity Training Project of Tianjin (201910065372).

■ REFERENCES

(1) Tarruell, L.; Greif, D.; Uehlinger, T.; Jotzu, G.; Esslinger, T. *Nature* **2012**, *483* (7389), 302.
(2) Novoselov, K. S.; Fal, V.; Colombo, L.; Gellert, P.; Schwab, M.; Kim, K. *Nature* **2012**, *490* (7419), 192.
(3) Liu, Y.; Dong, X.; Chen, P. *Chem. Soc. Rev.* **2012**, *41* (6), 2283–2307.
(4) Hajian, R.; Balderston, S.; Tran, T.; deBoer, T.; Etienne, J.; Sandhu, M.; Wauford, N. A.; Chung, J.-Y.; Nokes, J.; Athaiya, M.; Paredes, J.; Peytavi, R.; Goldsmith, B.; Murthy, N.; Conboy, I. M.; Aran, K. *Nat. Biomed. Eng.* **2019**, *3* (6), 427.
(5) Hao, Y.; Bharathi, M.; Wang, L.; Liu, Y.; Chen, H.; Nie, S.; Wang, X.; Chou, H.; Tan, C.; Fallahazad, B.; Ramanarayan, H.; Magnuson, C. W.; Tutuc, E.; Yakobson, B. I.; McCarty, K. F.; Zhang, Y.-W.; Kim, P.; Hone, J.; Colombo, L.; Ruoff, R. S. *Science* **2013**, *342* (6159), 720–723.
(6) Chen, J.-H.; Jang, C.; Adam, S.; Fuhrer, M.; Williams, E.; Ishigami, M. *Nat. Phys.* **2008**, *4* (5), 377.
(7) Martin, J.; Akerman, N.; Ulbricht, G.; Lohmann, T.; Smet, J. v.; von Klitzing, K.; Yacoby, A. *Nat. Phys.* **2008**, *4* (2), 144.
(8) Chen, J.-H.; Jang, C.; Xiao, S.; Ishigami, M.; Fuhrer, M. S. *Nat. Nanotechnol.* **2008**, *3* (4), 206.
(9) Lerner, M. B.; Matsunaga, F.; Han, G. H.; Hong, S. J.; Xi, J.; Crook, A.; Perez-Aguilar, J. M.; Park, Y. W.; Saven, J. G.; Liu, R.; Johnson, A. T. C. *Nano Lett.* **2014**, *14* (5), 2709–2714.
(10) Wang, C.; Li, Y.; Zhu, Y.; Zhou, X.; Lin, Q.; He, M. *Adv. Funct. Mater.* **2016**, *26* (42), 7668–7678.
(11) Jung, Y.; Choi, M. S.; Nipane, A.; Borah, A.; Kim, B.; Zangiabadi, A.; Taniguchi, T.; Watanabe, K.; Yoo, W. J.; Hone, J.; Teherani, J. T. *Nat. Electron.* **2019**, *2* (5), 187.
(12) Zhu, Y.; Wang, C.; Petrone, N.; Yu, J.; Nuckolls, C.; Hone, J.; Lin, Q. *Appl. Phys. Lett.* **2015**, *106* (12), 123503.
(13) Li, Y.; Wang, C.; Zhu, Y.; Zhou, X.; Xiang, Y.; He, M.; Zeng, S. *Biosens. Bioelectron.* **2017**, *89*, 758–763.
(14) Wang, C.; Ye, W.; Li, Y.; Zhu, Y.; Lin, Q.; He, M. *Biosens. Bioelectron.* **2019**, *129*, 93–99.
(15) Liu, J.; Lu, Y. *Org. Biomol. Chem.* **2006**, *4* (18), 3435–3441.
(16) Memon, A. G.; Zhou, X.; Xing, Y.; Wang, R.; Liu, L.; Khan, M.; He, M. *Front. Environ. Sci. Eng.* **2019**, *13* (1), 12.
(17) Han, S.; Zhou, X.; Tang, Y.; He, M.; Zhang, X.; Shi, H.; Xiang, Y. *Biosens. Bioelectron.* **2016**, *80*, 265–272.
(18) Lui, C. H.; Liu, L.; Mak, K. F.; Flynn, G. W.; Heinz, T. F. *Nature* **2009**, *462* (7271), 339.
(19) Shulaker, M. M.; Hills, G.; Patil, N.; Wei, H.; Chen, H.-Y.; Wong, H.-S. P.; Mitra, S. *Nature* **2013**, *501* (7468), 526.
(20) Huh, S.; Park, J.; Kim, Y. S.; Kim, K. S.; Hong, B. H.; Nam, J.-M. *ACS Nano* **2011**, *5* (12), 9799–9806.
(21) Vervuurt, R. H.; Kessels, W. M.; Bol, A. A. *Adv. Mater. Interfaces* **2017**, *4* (18), 1700232.
(22) George, S. M. *Chem. Rev.* **2010**, *110* (1), 111–131.
(23) Wang, Y.; Ho, M.-T.; Goncharova, L.; Wielunski, L.; Rivillon-Amy, S.; Chabal, Y.; Gustafsson, T.; Moumen, N.; Boleslawski, M. *Chem. Mater.* **2007**, *19* (13), 3127–3138.
(24) Wang, X.; Tabakman, S. M.; Dai, H. *J. Am. Chem. Soc.* **2008**, *130* (26), 8152–8153.
(25) Alaboson, J. M.; Wang, Q. H.; Emery, J. D.; Lipson, A. L.; Bedzyk, M. J.; Elam, J. W.; Pellin, M. J.; Hersam, M. C. *ACS Nano* **2011**, *5* (6), 5223–5232.
(26) Lee, B.; Park, S.-Y.; Kim, H.-C.; Cho, K.; Vogel, E. M.; Kim, M. J.; Wallace, R. M.; Kim, J. *Appl. Phys. Lett.* **2008**, *92* (20), 203102.

DOI: 10.1021/acs.nanolett.9b03528
Nano Lett. 2020, 20, 166–175

(27) McDonnell, S.; Pirkle, A.; Kim, J.; Colombo, L.; Wallace, R. M. *J. Appl. Phys.* **2012**, *112* (10), 104110.
(28) Xu, H.; Zhang, Z.; Wang, Z.; Wang, S.; Liang, X.; Peng, L.-M. *ACS Nano* **2011**, *5* (3), 2340−2347.
(29) Molinaro, R.; Corbo, C.; Martinez, J. O.; Taraballi, F.; Evangelopoulos, M.; Minardi, S.; Yazdi, I. K.; Zhao, P.; De Rosa, E.; Sherman, M.; De Vita, A.; Furman, N. E. T.; Wang, X.; Parodi, A.; Tasciotti, E. *Nat. Mater.* **2016**, *15* (9), 1037.
(30) Xia, J.; Chen, F.; Li, J.; Tao, N. *Nat. Nanotechnol.* **2009**, *4* (8), 505.
(31) Das, A.; Pisana, S.; Chakraborty, B.; Piscanec, S.; Saha, S. K.; Waghmare, U. V.; Novoselov, K. S.; Krishnamurthy, H. R.; Geim, A. K.; Ferrari, A. C.; Sood, A. K. *Nat. Nanotechnol.* **2008**, *3* (4), 210.
(32) Wang, L.; Meric, I.; Huang, P.; Gao, Q.; Gao, Y.; Tran, H.; Taniguchi, T.; Watanabe, K.; Campos, L.; Muller, D.; Guo, J.; Kim, P.; Hone, J.; Shepard, K. L.; Dean, C. R. *Science* **2013**, *342* (6158), 614−617.
(33) Schwierz, F. *Nat. Nanotechnol.* **2010**, *5* (7), 487.
(34) Meric, I.; Han, M. Y.; Young, A. F.; Özyilmaz, B.; Kim, P.; Shepard, K. L. *Nat. Nanotechnol.* **2008**, *3* (11), 654.
(35) Wang, H.; Wu, Y.; Cong, C.; Shang, J.; Yu, T. *ACS Nano* **2010**, *4* (12), 7221−7228.
(36) Zhu, Y.; Li, Y.; Arefe, G.; Burke, R. A.; Tan, C.; Hao, Y.; Liu, X.; Liu, X.; Yoo, W. J.; Dubey, M.; Lin, Q.; Hone, J. C. *Nano Lett.* **2018**, *18* (6), 3807−3813.
(37) Levesque, P. L.; Sabri, S. S.; Aguirre, C. M.; Guillemette, J.; Siaj, M.; Desjardins, P.; Szkopek, T.; Martel, R. *Nano Lett.* **2011**, *11* (1), 132−137.
(38) Ponomarenko, L.; Yang, R.; Mohiuddin, T.; Katsnelson, M.; Novoselov, K.; Morozov, S.; Zhukov, A.; Schedin, F.; Hill, E.; Geim, A. *Phys. Rev. Lett.* **2009**, *102* (20), 206603.
(39) Wang, C.; Kim, J.; Zhu, Y.; Yang, J.; Lee, G.-H.; Lee, S.; Yu, J.; Pei, R.; Liu, G.; Nuckolls, C.; Hone, J.; Lin, Q. *Biosens. Bioelectron.* **2015**, *71*, 222−229.
(40) Li, Y.; Zhu, Y.; Wang, C.; He, M.; Lin, Q. *Biosens. Bioelectron.* **2019**, *126*, 59−67.
(41) Wang, R.; Zhou, X.; Shi, H. *Biosens. Bioelectron.* **2015**, *74*, 78−84.
(42) Liu, H.; Yu, X.; Chen, Y.; Zhang, J.; Wu, B.; Zheng, L.; Haruehanroengra, P.; Wang, R.; Li, S.; Lin, J.; Li, J.; Sheng, J.; Huang, Z.; Ma, J.; Jianhua, G. *Nat. Commun.* **2017**, *8* (1), 2006.
(43) Fink, H.-W.; Schönenberger, C. *Nature* **1999**, *398* (6726), 407.
(44) Slinker, J. D.; Muren, N. B.; Renfrew, S. E.; Barton, J. K. *Nat. Chem.* **2011**, *3* (3), 228.
(45) Inkpen, M. S.; Liu, Z. F.; Li, H.; Campos, L. M.; Neaton, J. B.; Venkataraman, L. *Nat. Chem.* **2019**, *11* (4), 351.
(46) Chen, R. J.; Zhang, Y.; Wang, D.; Dai, H. *J. Am. Chem. Soc.* **2001**, *123* (16), 3838−3839.
(47) Sorgenfrei, S.; Chiu, C.-Y.; Johnston, M.; Nuckolls, C.; Shepard, K. L. *Nano Lett.* **2011**, *11* (9), 3739−3743.
(48) Gao, Y.; Wolf, L. K.; Georgiadis, R. M. *Nucleic Acids Res.* **2006**, *34* (11), 3370−3377.
(49) Sorgenfrei, S.; Chiu, C.-Y.; Gonzalez, R. L., Jr; Yu, Y.-J.; Kim, P.; Nuckolls, C.; Shepard, K. L. *Nat. Nanotechnol.* **2011**, *6* (2), 126.
(50) Schmickler, W. *Chem. Rev.* **1996**, *96* (8), 3177−3200.
(51) Nelson, B. P.; Grimsrud, T. E.; Liles, M. R.; Goodman, R. M.; Corn, R. M. *Anal. Chem.* **2001**, *73* (1), 1−7.
(52) Peterson, A. W.; Heaton, R. J.; Georgiadis, R. M. *Nucleic Acids Res.* **2001**, *29* (24), 5163−5168.
(53) Yu, F.; Yao, D.; Knoll, W. *Nucleic Acids Res.* **2004**, *32* (9), No. e75.
(54) Cui, L.; Liu, B.; Vonlanthen, D.; Mayor, M.; Fu, Y.; Li, J.-F.; Wandlowski, T. *J. Am. Chem. Soc.* **2011**, *133* (19), 7332−7335.
(55) Garner, M. H.; Li, H.; Chen, Y.; Su, T. A.; Shangguan, Z.; Paley, D. W.; Liu, T.; Ng, F.; Li, H.; Xiao, S.; Nuckolls, C.; Venkataraman, L.; Solomon, G. C. *Nature* **2018**, *558* (7710), 415.
(56) Homola, J. *Chem. Rev.* **2008**, *108* (2), 462−493.

DOI: 10.1021/acs.nanolett.9b03528
Nano Lett. 2020, 20, 166−175